

Atmospheric and Astrophysical Neutrinos above 1 TeV Interacting in IceCube

M. G. Aartsen,² M. Ackermann,⁴⁸ J. Adams,¹⁵ J. A. Aguilar,²³ M. Ahlers,²⁸ M. Ahrens,³⁸ D. Altmann,²² T. Anderson,⁴⁴ C. Argüelles,²⁸ T. C. Arlen,⁴⁴ J. Auffenberg,¹ X. Bai,³⁶ S. W. Barwick,²⁵ V. Baum,²⁹ R. Bay,⁷ J. J. Beatty,^{17,18} J. Becker Tjus,¹⁰ K.-H. Becker,⁴⁶ S. BenZvi,²⁸ P. Berghaus,⁴⁸ D. Berley,¹⁶ E. Bernardini,⁴⁸ A. Bernhard,³² D. Z. Besson,²⁶ G. Binder,^{8,7} D. Bindig,⁴⁶ M. Bissok,¹ E. Blaufuss,¹⁶ J. Blumenthal,¹ D. J. Boersma,⁴⁵ C. Bohm,³⁸ F. Bos,¹⁰ D. Bose,⁴⁰ S. Böser,¹¹ O. Botner,⁴⁵ L. Brayeur,¹³ H.-P. Bretz,⁴⁸ A. M. Brown,¹⁵ N. Buzinsky,²¹ J. Casey,⁵ M. Casier,¹³ E. Cheung,¹⁶ D. Chirkin,²⁸ A. Christov,²³ B. Christy,¹⁶ K. Clark,⁴¹ L. Classen,²² F. Clevermann,²⁰ S. Coenders,³² D. F. Cowen,^{44,43} A. H. Cruz Silva,⁴⁸ M. Danninger,³⁸ J. Daughhetee,⁵ J. C. Davis,¹⁷ M. Day,²⁸ J. P. A. M. de André,⁴⁴ C. De Clercq,¹³ S. De Ridder,²⁴ P. Desiati,²⁸ K. D. de Vries,¹³ M. de With,⁹ T. DeYoung,³⁰ J. C. Díaz-Vélez,²⁸ M. Dunkman,⁴⁴ R. Eagan,⁴⁴ B. Eberhardt,²⁹ B. Eichmann,¹⁰ J. Eisch,²⁸ S. Euler,⁴⁵ P. A. Evenson,³³ O. Fadiran,²⁸ A. R. Fazely,⁶ A. Fedynitch,¹⁰ J. Feintzeig,²⁸ J. Felde,¹⁶ T. Feusels,²⁴ K. Filimonov,⁷ C. Finley,³⁸ T. Fischer-Wasels,⁴⁶ S. Flis,³⁸ A. Franckowiak,¹¹ K. Frantzen,²⁰ T. Fuchs,²⁰ T. K. Gaisser,³³ R. Gaior,¹⁴ J. Gallagher,²⁷ L. Gerhardt,^{8,7} D. Gier,¹ L. Gladstone,²⁸ T. Glüsenskamp,⁴⁸ A. Goldschmidt,⁸ G. Golup,¹³ J. G. Gonzalez,³³ J. A. Goodman,¹⁶ D. Góra,⁴⁸ D. Grant,²¹ P. Gresskov,¹ J. C. Groh,⁴⁴ A. Groß,³² C. Ha,^{8,7} C. Haack,¹ A. Haj Ismail,²⁴ P. Hallen,¹ A. Hallgren,⁴⁵ F. Halzen,²⁸ K. Hanson,¹² D. Hebecker,¹¹ D. Heereman,¹² D. Heinen,¹ K. Helbing,⁴⁶ R. Hellauer,¹⁶ D. Hellwig,¹ S. Hickford,¹⁵ G. C. Hill,² K. D. Hoffman,¹⁶ R. Hoffmann,⁴⁶ A. Homeier,¹¹ K. Hoshina,^{28,*} F. Huang,⁴⁴ W. Huelsnitz,¹⁶ P. O. Hulth,³⁸ K. Hultqvist,³⁸ S. Hussain,³³ A. Ishihara,¹⁴ E. Jacobi,⁴⁸ J. Jacobsen,²⁸ K. Jagielski,¹ G. S. Japaridze,⁴ K. Jero,²⁸ O. Jlelati,²⁴ M. Jurkovic,³² B. Kaminsky,⁴⁸ A. Kappes,²² T. Karg,⁴⁸ A. Karle,²⁸ M. Kauer,^{28,47} A. Keivani,⁴⁴ J. L. Kelley,²⁸ A. Kheirandish,²⁸ J. Kiryluk,³⁹ J. Kläs,⁴⁶ S. R. Klein,^{8,7} J.-H. Köhne,²⁰ G. Kohnen,³¹ H. Kolanoski,⁹ A. Koob,¹ L. Köpke,²⁹ C. Kopper,²¹ S. Kopper,⁴⁶ D. J. Koskinen,¹⁹ M. Kowalski,¹¹ A. Kriesten,¹ K. Krings,¹ G. Kroll,²⁹ M. Kroll,¹⁰ J. Kunnen,¹³ N. Kurahashi,³⁵ T. Kuwabara,¹⁴ M. Labare,²⁴ D. T. Larsen,²⁸ M. J. Larson,¹⁹ M. Lesiak-Bzdak,³⁹ M. Leuermann,¹ J. Leute,³² J. Lünemann,¹³ J. Madsen,³⁷ G. Maggi,¹³ R. Maruyama,⁴⁷ K. Mase,¹⁴ H. S. Matis,⁸ R. Maunu,¹⁶ F. McNally,²⁸ K. Meagher,¹⁶ M. Medici,¹⁹ A. Meli,²⁴ T. Meures,¹² S. Miarecki,^{8,7} E. Middell,⁴⁸ E. Middlemas,²⁸ N. Milke,²⁰ J. Miller,¹³ L. Mohrmann,⁴⁸ T. Montaruli,²³ R. Morse,²⁸ R. Nahnauer,⁴⁸ U. Naumann,⁴⁶ H. Niederhausen,³⁹ S. C. Nowicki,²¹ D. R. Nygren,⁸ A. Obertacke,⁴⁶ S. Odrowski,²¹ A. Olivas,¹⁶ A. Omairat,⁴⁶ A. O'Murchadha,¹² T. Palczewski,⁴² L. Paul,¹ Ö. Penek,¹ J. A. Pepper,⁴² C. Pérez de los Heros,⁴⁵ C. Pfendner,¹⁷ D. Pieloth,²⁰ E. Pinat,¹² J. Posselt,⁴⁶ P. B. Price,⁷ G. T. Przybylski,⁸ J. Pütz,¹ M. Quinnan,⁴⁴ L. Rädcl,¹ M. Rameez,²³ K. Rawlins,³ P. Redl,¹⁶ I. Rees,²⁸ R. Reimann,¹ M. Relich,¹⁴ E. Resconi,³² W. Rhode,²⁰ M. Richman,¹⁶ B. Riedel,²⁸ S. Robertson,² J. P. Rodrigues,²⁸ M. Rongen,¹ C. Rott,⁴⁰ T. Ruhe,²⁰ B. Ruzybayev,³³ D. Ryckbosch,²⁴ S. M. Saba,¹⁰ H.-G. Sander,²⁹ J. Sandroos,¹⁹ M. Santander,²⁸ S. Sarkar,^{19,34} K. Schatto,²⁹ F. Scheriau,²⁰ T. Schmidt,¹⁶ M. Schmitz,²⁰ S. Schoenen,¹ S. Schöneberg,¹⁰ A. Schönwald,⁴⁸ A. Schukraft,¹ L. Schulte,¹¹ O. Schulz,³² D. Seckel,³³ Y. Sestayo,³² S. Seunarine,³⁷ R. Shanidze,⁴⁸ M. W. E. Smith,⁴⁴ D. Soldin,⁴⁶ G. M. Spiczak,³⁷ C. Spiering,⁴⁸ M. Stamatikos,^{17,†} T. Stanev,³³ N. A. Stanisha,⁴⁴ A. Stasik,¹¹ T. Stezelberger,⁸ R. G. Stokstad,⁸ A. Stöbl,⁴⁸ E. A. Strahler,¹³ R. Ström,⁴⁵ N. L. Strotjohann,¹¹ G. W. Sullivan,¹⁶ H. Taavola,⁴⁵ I. Taboada,⁵ A. Tamburro,³³ A. Tepe,⁴⁶ S. Ter-Antonyan,⁶ A. Terliuk,⁴⁸ G. Tešić,⁴⁴ S. Tilav,³³ P. A. Toale,⁴² M. N. Tobin,²⁸ D. Tosi,²⁸ M. Tselengidou,²² E. Unger,⁴⁵ M. Usner,¹¹ S. Vallecorsa,²³ N. van Eijndhoven,¹³ J. Vandenbroucke,²⁸ J. van Santen,^{28,‡} M. Vehring,¹ M. Voge,¹¹ M. Vraeghe,²⁴ C. Walck,³⁸ M. Wallraff,¹ Ch. Weaver,²⁸ M. Wellons,²⁸ C. Wendt,²⁸ S. Westerhoff,²⁸ B. J. Whelan,² N. Whitehorn,²⁸ C. Wichary,¹ K. Wiebe,²⁹ C. H. Wiebusch,¹ D. R. Williams,⁴² H. Wissing,¹⁶ M. Wolf,³⁸ T. R. Wood,²¹ K. Woschnagg,⁷ D. L. Xu,⁴² X. W. Xu,⁶ J. P. Yanez,⁴⁸ G. Yodh,²⁵ S. Yoshida,¹⁴ P. Zarzhitsky,⁴² J. Ziemann,²⁰ S. Zierke,¹ and M. Zoll³⁸

¹*III. Physikalisches Institut, RWTH Aachen University, D-52056 Aachen, Germany*

²*School of Chemistry & Physics, University of Adelaide, Adelaide SA, 5005 Australia*

³*Dept. of Physics and Astronomy, University of Alaska Anchorage, 3211 Providence Dr., Anchorage, AK 99508, USA*

⁴*CTSPS, Clark-Atlanta University, Atlanta, GA 30314, USA*

⁵*School of Physics and Center for Relativistic Astrophysics, Georgia Institute of Technology, Atlanta, GA 30332, USA*

⁶*Dept. of Physics, Southern University, Baton Rouge, LA 70813, USA*

⁷*Dept. of Physics, University of California, Berkeley, CA 94720, USA*

⁸*Lawrence Berkeley National Laboratory, Berkeley, CA 94720, USA*

⁹*Institut für Physik, Humboldt-Universität zu Berlin, D-12489 Berlin, Germany*

¹⁰*Fakultät für Physik & Astronomie, Ruhr-Universität Bochum, D-44780 Bochum, Germany*

- ¹¹Physikalisches Institut, Universität Bonn, Nussallee 12, D-53115 Bonn, Germany
- ¹²Université Libre de Bruxelles, Science Faculty CP230, B-1050 Brussels, Belgium
- ¹³Vrije Universiteit Brussel, Dienst ELEM, B-1050 Brussels, Belgium
- ¹⁴Dept. of Physics, Chiba University, Chiba 263-8522, Japan
- ¹⁵Dept. of Physics and Astronomy, University of Canterbury, Private Bag 4800, Christchurch, New Zealand
- ¹⁶Dept. of Physics, University of Maryland, College Park, MD 20742, USA
- ¹⁷Dept. of Physics and Center for Cosmology and Astro-Particle Physics, Ohio State University, Columbus, OH 43210, USA
- ¹⁸Dept. of Astronomy, Ohio State University, Columbus, OH 43210, USA
- ¹⁹Niels Bohr Institute, University of Copenhagen, DK-2100 Copenhagen, Denmark
- ²⁰Dept. of Physics, TU Dortmund University, D-44221 Dortmund, Germany
- ²¹Dept. of Physics, University of Alberta, Edmonton, Alberta, Canada T6G 2E1
- ²²Erlangen Centre for Astroparticle Physics, Friedrich-Alexander-Universität Erlangen-Nürnberg, D-91058 Erlangen, Germany
- ²³Département de physique nucléaire et corpusculaire, Université de Genève, CH-1211 Genève, Switzerland
- ²⁴Dept. of Physics and Astronomy, University of Gent, B-9000 Gent, Belgium
- ²⁵Dept. of Physics and Astronomy, University of California, Irvine, CA 92697, USA
- ²⁶Dept. of Physics and Astronomy, University of Kansas, Lawrence, KS 66045, USA
- ²⁷Dept. of Astronomy, University of Wisconsin, Madison, WI 53706, USA
- ²⁸Dept. of Physics and Wisconsin IceCube Particle Astrophysics Center, University of Wisconsin, Madison, WI 53706, USA
- ²⁹Institute of Physics, University of Mainz, Staudinger Weg 7, D-55099 Mainz, Germany
- ³⁰Dept. of Physics and Astronomy, Michigan State University, East Lansing, MI 48824, USA
- ³¹Université de Mons, 7000 Mons, Belgium
- ³²Technische Universität München, D-85748 Garching, Germany
- ³³Bartol Research Institute and Dept. of Physics and Astronomy, University of Delaware, Newark, DE 19716, USA
- ³⁴Dept. of Physics, University of Oxford, 1 Keble Road, Oxford OX1 3NP, UK
- ³⁵Dept. of Physics, Drexel University, 3141 Chestnut Street, Philadelphia, PA 19104, USA
- ³⁶Physics Department, South Dakota School of Mines and Technology, Rapid City, SD 57701, USA
- ³⁷Dept. of Physics, University of Wisconsin, River Falls, WI 54022, USA
- ³⁸Oskar Klein Centre and Dept. of Physics, Stockholm University, SE-10691 Stockholm, Sweden
- ³⁹Dept. of Physics and Astronomy, Stony Brook University, Stony Brook, NY 11794-3800, USA
- ⁴⁰Dept. of Physics, Sungkyunkwan University, Suwon 440-746, Korea
- ⁴¹Dept. of Physics, University of Toronto, Toronto, Ontario, Canada, M5S 1A7
- ⁴²Dept. of Physics and Astronomy, University of Alabama, Tuscaloosa, AL 35487, USA
- ⁴³Dept. of Astronomy and Astrophysics, Pennsylvania State University, University Park, PA 16802, USA
- ⁴⁴Dept. of Physics, Pennsylvania State University, University Park, PA 16802, USA
- ⁴⁵Dept. of Physics and Astronomy, Uppsala University, Box 516, S-75120 Uppsala, Sweden
- ⁴⁶Dept. of Physics, University of Wuppertal, D-42119 Wuppertal, Germany
- ⁴⁷Dept. of Physics, Yale University, New Haven, CT 06520, USA
- ⁴⁸DESY, D-15735 Zeuthen, Germany

The IceCube Neutrino Observatory was designed primarily to search for high-energy (TeV–PeV) neutrinos produced in distant astrophysical objects. A search for $\gtrsim 100$ TeV neutrinos interacting inside the instrumented volume has recently provided evidence for an isotropic flux of such neutrinos. At lower energies, IceCube collects large numbers of neutrinos from the weak decays of mesons in cosmic-ray air showers. Here we present the results of a search for neutrino interactions inside IceCube’s instrumented volume between 1 TeV and 1 PeV in 641 days of data taken from 2010–2012, lowering the energy threshold for neutrinos from the southern sky below 10 TeV for the first time, far below the threshold of the previous high-energy analysis. Astrophysical neutrinos remain the dominant component in the southern sky down to a deposited energy of 10 TeV. From these data we derive new constraints on the diffuse astrophysical neutrino spectrum, $\Phi_\nu = 2.06_{-0.3}^{+0.4} \times 10^{-18} (E_\nu/10^5 \text{ GeV})^{-2.46 \pm 0.12} \text{ GeV}^{-1} \text{ cm}^{-2} \text{ sr}^{-1} \text{ s}^{-1}$ for $25 \text{ TeV} < E_\nu < 1.4 \text{ PeV}$, as well as the strongest upper limit yet on the flux of neutrinos from charmed-meson decay in the atmosphere, 1.52 times the benchmark theoretical prediction used in previous IceCube results at 90% confidence.

* Earthquake Research Institute, University of Tokyo, Bunkyo, Tokyo 113-0032, Japan

† NASA Goddard Space Flight Center, Greenbelt, MD 20771, USA

‡ Corresponding author; jvansanten@icecube.wisc.edu

I. INTRODUCTION

High-energy neutrinos are ideal cosmic messengers, produced whenever cosmic rays interact with matter or photons near their as-yet unknown acceleration sites, and carrying information about the conditions there to Earth without being deflected by magnetic fields or absorbed by intervening matter [1–4]. At the same time, neutrinos produced in cosmic-ray air showers provide information about hadronic physics in kinematic regions that are difficult to probe with terrestrial accelerators. Here we present an analysis of the diffuse flux of neutrinos observed from 2010–2012 via events with vertices contained in the IceCube detector [5] and depositing more than 1 TeV of energy. We derive new constraints on the energy spectrum of the previously-observed [6, 7] astrophysical neutrino flux as well as the maximum contribution from the decay of charmed mesons in the atmosphere covering significantly lower energies. This will allow further limits on the possible scenarios [8–17] that have been put forward to explain the observed astrophysical flux.

In the first section, we review the sources of neutrinos that can be observed in IceCube, the signatures of neutrino interactions, and general methods for separating neutrino events from the extremely large background of penetrating atmospheric muons. Then, we present the veto techniques used to isolate a neutrino-dominated data sample with sensitivity to neutrinos of all flavors coming from all directions and the analysis technique that will be applied to the sample to infer the properties of the underlying neutrino fluxes. Finally, we present the results of the search and analysis before discussing the implications of the result and directions for future searches.

A. Sources of TeV neutrinos at Earth

Neutrinos are an inevitable byproduct of high-energy hadronic interactions that produce weakly-decaying mesons. They may be produced either within cosmic-ray-induced air showers, giving rise to a flux of atmospheric neutrinos [18–29], or in the vicinity of distant astrophysical accelerators, giving rise to a flux of astrophysical neutrinos [30–51].

The largest contribution to the atmospheric neutrino flux comes from 2-body decays of charged pions and kaons. These decays produce ν_μ almost exclusively because of the chiral structure of the weak interaction [52]. IceCube has observed this flux from the northern sky¹ with high statistics [53], and its normalization, angular

distribution, and spectral shape agree well with theoretical predictions [22]. Because the decays that produce ν_μ also produce muons of similar or greater energy, high-energy atmospheric ν_μ from the southern sky are often accompanied by penetrating muons [54]. This is a useful property that can be used to distinguish them from astrophysical neutrinos, which are never accompanied by muons.

The flux of TeV atmospheric ν_e is much smaller, arising primarily from 3-body decays of K^\pm and K_L^0 [52, 55]. This flux has also been observed in IceCube up to a few TeV as an excess of events over the predicted rate from interactions of atmospheric ν_μ in the more densely-instrumented DeepCore subarray [56]. In the southern sky these too are often accompanied by muons, though the accompanied fraction is smaller because the muons must come from the decays of other mesons in the air shower [57].

A third contribution to the atmospheric neutrino flux observable in IceCube is predicted to come from the decays of heavy, very short-lived mesons containing charm quarks like the D^\pm . These decay preferentially to 3-body final states, with nearly equal branching ratios to ν_μ and ν_e [58]. In addition, their prompt decay (on the order of a picosecond) makes re-interaction extremely unlikely, so the energy spectrum of neutrinos from charmed meson decay follows that of the cosmic rays up to 50 PeV and is independent of the local density of the atmosphere at production altitude [52]. This prompt flux has not yet been conclusively observed in either muons or neutrinos, and predictions for the normalization of the prompt atmospheric neutrino flux vary widely [27, 28], though more optimistic models [59] have already been excluded by IceCube measurements [53]. Like neutrinos from light meson decays, neutrinos from charmed meson decay are accompanied by muons. For ν_μ the accompanied fraction is similar to that in pion and kaon decays. For ν_e it is slightly lower, because charmed meson decays are more likely than kaon decays to produce high-energy neutrinos in relatively low-energy, muon-poor showers [57].

While the interactions of cosmic-ray nuclei with the Earth’s atmosphere are the largest source of high-energy neutrinos, these nuclei must come from some population of sources. Interactions with matter or radiation fields in the vicinity of those sources will produce neutrinos. Diffusive shock acceleration is the most promising mechanism for accelerating protons to the energies observed in the cosmic ray spectrum above the knee; under fairly general conditions this is expected to produce a flux of protons with a power-law spectrum at the source similar to $dN/dE \propto E^{-2}$ [1, 2, 4, 60]. When these protons interact with other protons near the source, they produce charged pions that decay to produce ν_μ and μ that in turn decay to produce further ν_μ and ν_e . Long-baseline oscillations will transform this $\nu_e : \nu_\mu : \nu_\tau$ ratio from 1 : 2 : 0 into approximately 1 : 1 : 1 at Earth [61, 62]. Unless the source environment is very dense, the energy spectrum of these astrophysical neutrinos follows that of

¹ The “north” and “south” denote halves of the celestial sphere as observed from the Geographic South Pole rather than terrestrial hemispheres. The majority of atmospheric neutrinos observed from the northern sky are produced in air showers that reach ground level at points in the southern terrestrial hemisphere.

the progenitor protons ($\sim E^{-2}$), so their flux exceeds that of the atmospheric neutrinos at sufficiently high energies. Unlike atmospheric neutrinos, astrophysical neutrinos always arrive without accompanying muons.

B. Neutrino detection in IceCube

The IceCube detector [5, 63] can detect neutrinos of all flavors by observing the Cherenkov photons induced by the charged end products of charged- or neutral-current deep-inelastic neutrino-nucleon scattering in the ice. The signatures of these interactions fall into two broad categories: “tracks,” due to charged-current (CC) ν_μ scattering and “cascades,” due to CC interactions of ν_e as well as neutral-current (NC) interactions of all flavors². Detections of these event signatures and reconstruction of their properties may be used to infer the angular, energy, and flavor distribution of an observed neutrino flux.

Roughly 1/3 of neutrino interactions at a given energy will be neutral-current scatterings, where the neutrino transfers on average $\sim 1/3$ of its kinetic energy to a quark in the target nucleus [65], producing a short (~ 5 m) shower of relativistic charged particles. If the neutrino vertex is inside or sufficiently close to the instrumented volume, the Cherenkov radiation they induce may be detected and used to reconstruct the vertex position and deposited energy, and to some degree the direction. The remaining 2/3 of interactions are charged-current scatterings that produce a charged lepton of the same flavor as the incident neutrino in addition to a hadronic shower. While nearly all of the neutrino’s energy is converted to relativistic charged particles, the accuracy with which the direction and energy of the incident neutrino may be reconstructed depends strongly on the lepton flavor. Electrons induce short electromagnetic showers whose energy can be reconstructed to within 10% above 10 TeV if fully inside the instrumented volume [64]. The direction of the shower may also be inferred by matching the spatial and temporal pattern of detected photons to a template of its angular emission profile, though the short scattering length of the glacial ice at the South Pole limits the angular resolution to $\sim 10^\circ$ even above 100 TeV [64]. Muons lose energy much less quickly, and so can traverse kilometers of ice. While this makes it possible to positively identify ν_μ CC interactions and reconstruct their direction to within 1° [53, 66], it is more difficult to infer the initial neutrino energy when only a segment of the muon track can be observed.

The background to neutrino searches comes from atmospheric muons that penetrate the 1.5 km of ice overburden; they outnumber neutrino interactions by a factor of $\sim 10^6$. The traditional method of separating neutrino events from the penetrating muon background is to select only events where a muon comes from below the horizon, where the bulk of the Earth completely absorbs atmospheric muons. While this makes the effective volume of the detector much larger than its geometrical volume, the method is only sensitive to CC ν_μ interactions and cannot be extended much more than $\sim 5^\circ$ above the geometric horizon before penetrating muons begin to overwhelm neutrino-induced ones. An alternative approach is to select events that start inside the instrumented volume: neutrinos are completely invisible, whereas incoming muons induce Cherenkov photons that should be detected as the muon enters the fiducial volume. Such a veto-based event selection can be sensitive to neutrinos of all flavors from all directions, though it must sacrifice some effective volume to implement the veto. Since a muon veto also rejects down-going atmospheric neutrinos that are accompanied by muons, a veto-based event selection also enjoys a smaller atmospheric neutrino background than the traditional up-going neutrino selection [54], as illustrated in Fig. 1.

II. EVENT SELECTION

Active vetoes have been used in IceCube to isolate neutrino interactions inside the instrumented volume of the detector before. The method has been used effectively in the DeepCore subarray [56] and in the full detector above 100 TeV [6, 7]³. However, it has not been explored in the region between 10 and 100 TeV, where neutrinos from charmed meson decay in the atmosphere should be observable. Extending veto methods to this intermediate energy range without sacrificing sensitivity to all neutrino flavors or to neutrinos from the southern sky requires new techniques. Figure 2 illustrates the effects of the three stages of the event selection that will be described in this section: a pre-selection cut to reduce the data rate to a manageable level, veto cuts to remove events with signs of incoming muons, and a fiducial volume cut to remove events where incoming muons cannot be vetoed with sufficiently high probability.

A. Data collection and pre-selection

The IceCube detector [5, 63] consists of 5160 Digital Optical Modules (DOMs) buried in the glacial ice at the

² While CC ν_τ interactions also produce a τ track, the brief lifetime of the τ makes it too short to be observable on the scale of IceCube below a few tens of PeV [64]. Also, if a CC ν_μ interaction occurs inside the instrumented volume, it will appear more track-like or more cascade-like depending on inelasticity of the interaction and the path of the outgoing muon.

³ Veto methods were also used in previous searches for cascade events in AMANDA and IceCube [67–70], but were not the primary method of background rejection.

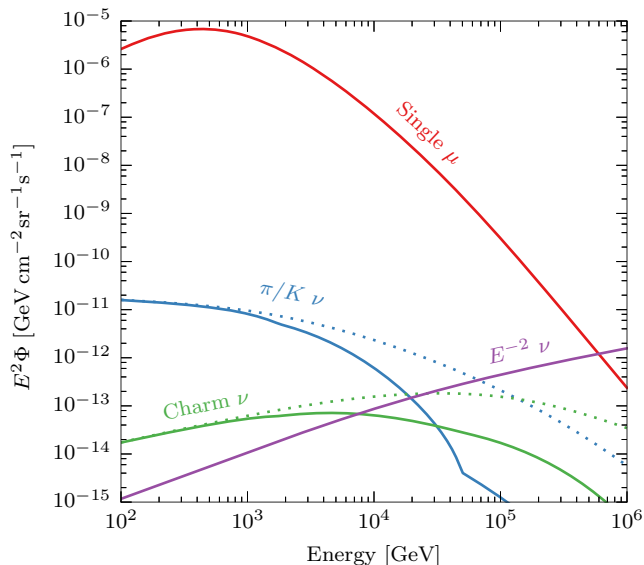


FIG. 1. Fluxes of vertically-downgoing muons and neutrinos detectable in IceCube. The upper line shows the flux of penetrating, single atmospheric muons at the depth of IceCube, while the remaining lines show neutrino fluxes multiplied by the probability that a neutrino of the given energy would interact in 1 km of glacial ice. The dotted lines show the total interacting flux of atmospheric neutrinos of all flavors [19, 28], while the corresponding solid lines show the interacting flux that arrives at the depth of IceCube without accompanying muons above 1 TeV [57]. Accompanying muons suppress the effective ν_μ flux from π and K decay below the level of the effective ν_e flux from K decay at 50 TeV, producing a kink in the spectrum. The E^{-2} astrophysical neutrino flux, shown here with the normalization of [7], always arrives without accompanying muons.

South Pole, instrumenting a total volume of approximately 1 km^3 . The DOMs are attached to cables that provide power and communication with the data acquisition system on the surface of the glacier. Each of these “strings” hosts 60 DOMs; 78 of the strings are spaced 125 m apart on a hexagonal grid with DOMs placed every 17 m from 1450 to 2450 m below the surface, while the remaining 8 strings form the DeepCore in-fill array [63]. These in-fill strings are 30–60 m from the nearest string with 50 DOMs placed every 7 m between 2100 and 2450 m below the surface, where the glacial ice is most transparent, and 10 DOMs placed every 10 m between 1750 and 1850 m below the surface. The data that will be presented in Sec. IV were taken with the nearly-complete 79-string detector configuration from May 2010 to May 2011 and the first year of the complete 86-string detector from May 2011 to May 2012.

Each DOM consists of a 25 cm diameter photomultiplier tube (PMT) [71], power supply, and digitization electronics housed in a borosilicate glass pressure sphere. The PMT signal is digitized and stored for transmission to the surface whenever the PMT output current exceeds $1/4$ of the mean peak current of the pulse amplified from

a single photo-electron (PE); if a neighboring or next-to-neighboring DOM on the same string also triggers within $1 \mu\text{s}$ (local coincidence) the readout extends for $6.4 \mu\text{s}$, otherwise the readout only includes a 75 ns window around the peak current in the first 400 ns after the local trigger. The digitized waveforms are transmitted to the surface, where they are assembled into events by a software trigger [5, 72].

The arrival times of individual photons and photon bunches are reconstructed by deconvolving the characteristic single-PE pulse shape from the digitized waveforms [64], and the resulting times and photon counts are used to reconstruct the vertices, directions, and energies [64, 66] of the relativistic charged particles that induced the detected Cherenkov photons.

The first stage of the event selection is done at the South Pole to reduce the data rate enough for transmission over a satellite link; the resulting sample, shown in the left panel of Fig. 2, includes $\sim 1\%$ of all triggering events. While this selection retains the majority of triggering neutrino events, they are still out-numbered 10,000 to 1 by penetrating muons. The remaining selection steps remove this background, leaving a nearly-pure sample of neutrino events.

B. Veto

This selection targets interactions of isolated neutrinos that occur inside the instrumented volume, producing a cascade at the neutrino vertex as well as an out-going track in the case of CC ν_μ . These can be distinguished from incoming muons (and atmospheric neutrinos accompanied by muons) by photons detected before the putative neutrino vertex. The simplest approach is the one employed in [6], where the outermost layer of PMTs is used as an active veto. The event is rejected if photons are detected on the outermost layer before the estimated vertex time. Spurious vetoes due to detector noise are mitigated by requiring that the photons are detected in local coincidence [5] at times that are causally compatible with the estimated vertex. For very bright events with thousands of detected photons, this single cut is sufficient to suppress the muon background below the level of atmospheric neutrinos (Fig. 2, center panel).

As the energy threshold is lowered, the number of background muons increases rapidly, while their average energy loss rate decreases, a combination that overwhelms the ability of the single layer to reject incoming muons. In order to extend the selection to lower energies, a second kind of veto, similar to those employed in [56, 73], is required. The first modification is to remove the requirements that veto photons be detected on the outermost layer of PMTs and in local coincidence. This allows isolated photon detections anywhere in the instrumented volume to veto an incoming track, which lowers the energy threshold but also loses signal events to spurious vetoes caused by noise. In order to mitigate the signal

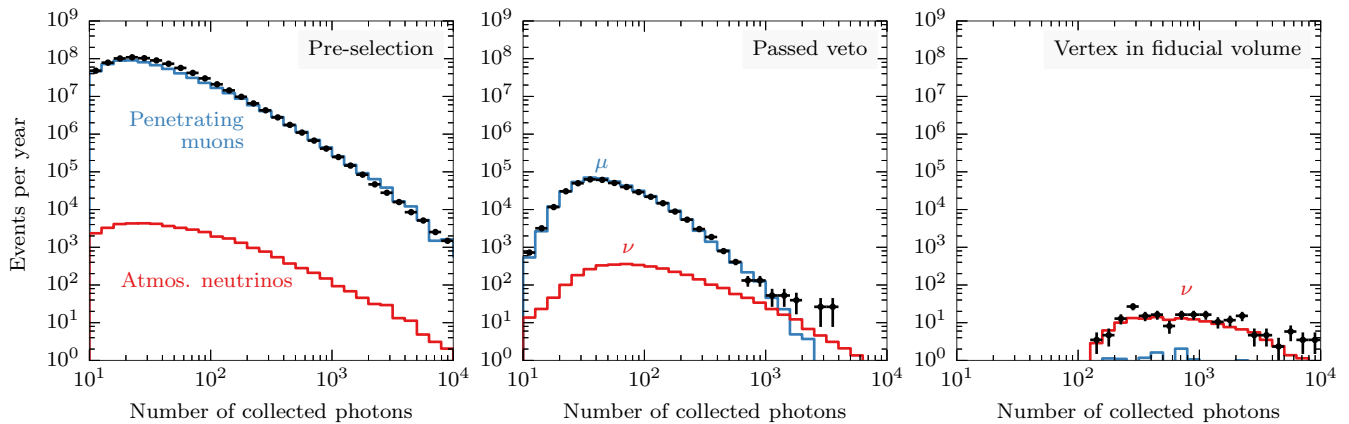


FIG. 2. Distribution of photon counts per event after each stage of the event selection. The total number of collected photons is on average proportional to the total deposited energy; for example, 10^3 photons correspond to roughly 10 TeV deposited energy. The stepped lines show the prediction from Monte Carlo simulation of penetrating atmospheric muons (blue) atmospheric neutrinos (red), while the points show experimental data. Left: Pre-selected events transmitted from the South Pole (Sec. II A). Center: Removed events with veto hits (Sec. II B). Right: Fiducial volume scaled with photon count (Sec. II C).

loss, a second modification is required: photons are only considered for veto if they are detected at a time and position consistent with an incoming track but inconsistent with the reconstructed cascade vertex, as shown in Fig. 3a.

The most resilient background comes from single muons with a single disproportionately large stochastic energy loss. Such events can be completely dominated by the photons induced by the largest energy loss, causing track reconstruction algorithms that assume uniform light emission to fail to find the correct direction. The position and time of the vertex can, however, be reconstructed reliably regardless of the presence of a muon track. In order to ensure that veto photons will be found, the search is repeated for each of 104 different down-going track hypotheses⁴ that pass through the reconstructed vertex. The track hypothesis with the largest number of associated veto photons is considered the best. A photon is associated with an incoming track if it is detected

- at least 50 ns before the earliest possible time for a photon induced at the previously reconstructed vertex,
- between 15 ns before and 1000 ns after the earliest possible time for a photon induced by the hypothetical muon,
- and no more than 100 m from the hypothetical muon trajectory.

The event is rejected if the best track has more than two associated photons.

⁴ The directions are chosen from the upper hemisphere of a HEALpix [74] grid.

C. Fiducial volume scaling

Since the effectiveness of the track-based veto is proportional to the probability of detecting at least 2 photons from an incoming muon before the reconstructed vertex, it increases in proportion to the number of detectable photons the muon induces and the number of PMTs it passes on its way to the vertex as shown in Fig. 4. This relationship can be exploited to maintain sufficient penetrating muon rejection at low energies by requiring a minimum distance between the reconstructed vertex and the edges of the instrumented volume that increases as the number of collected photons decreases as shown in Fig. 5. At the lowest photon counts the fiducial volume is reduced to the DeepCore subarray with the remainder of the detector used as a veto; as the photon count increases the veto reduces to the outermost layer of PMTs as in [6]. This selection creates the neutrino-dominated sample shown in the right panel of Figure 2. Tables of the effective area of this selection as a function of incident neutrino energy and zenith angle are provided in the online supplemental materials for this article.

III. ANALYSIS METHOD

The events that pass the selection defined above arise from four sources: conventional atmospheric neutrinos, prompt atmospheric neutrinos, penetrating atmospheric muons, and high-energy extraterrestrial neutrinos. Each of these components produces a distinct distribution in the observables chosen for this analysis: reconstructed deposited energy, reconstructed zenith angle, and the presence or absence of a detectable outgoing muon track. We disentangle the contributions of each of these components by fitting a model of their observable distribu-

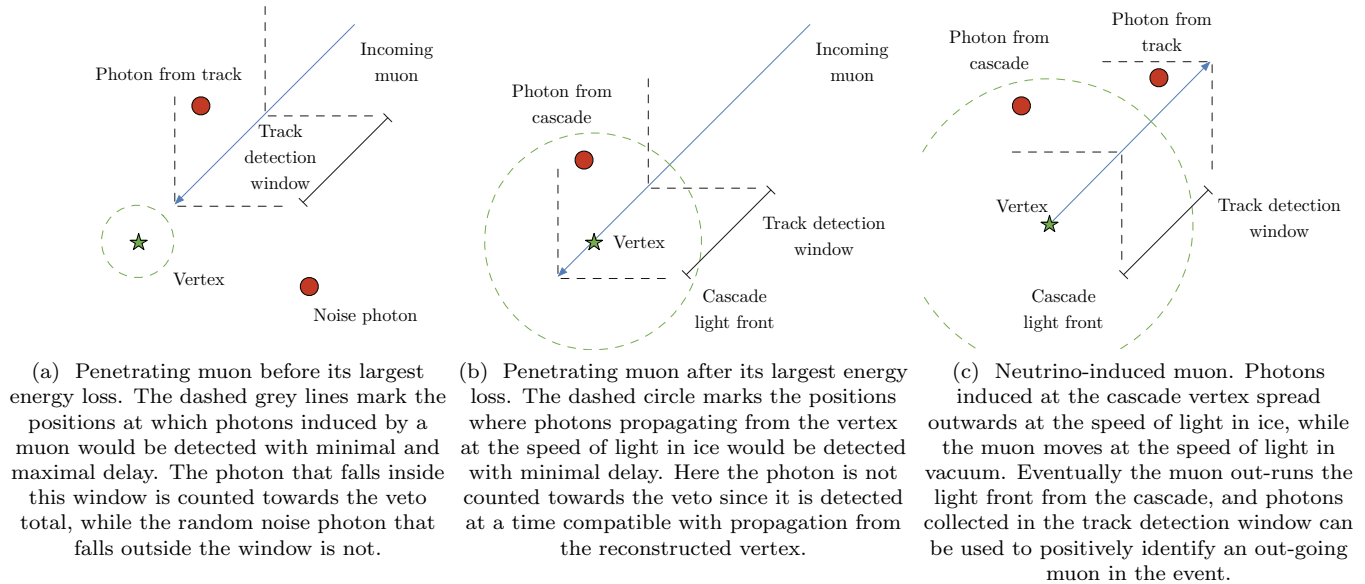


FIG. 3. An illustration of the incoming-muon veto procedure described in Sec. II B. Each panel shows a snapshot in time with the current position of the muon marked by the blue arrowhead and the position of the reconstructed vertex marked by a green star. (a) shows a penetrating muon before its largest energy loss with a photon detection that counts towards the veto, while (b) shows the same configuration after the largest energy loss with an ambiguous photon detection that does not count towards the veto. (c) shows how the technique can be inverted to detect starting tracks.

tions predicted from Monte Carlo simulation to the observed data. In this section we define the observables and discuss their expected distributions for each component. Then, we present the likelihood fitting technique and the method for determining statistical errors on the fit parameters.

The deposited energy is reconstructed by fitting the observed spatial and temporal distribution of detected photons to a template derived from simulations of single, point-like electromagnetic cascades as described in [64]. This electromagnetic-equivalent energy can be resolved to within 10% (68% C.L.) and is a proxy for the neutrino energy; for CC ν_e it is a nearly unbiased estimator of the neutrino energy [75], while for all other interaction types it is on average proportional to the neutrino energy. Since the template depends on the orientation of the cascade with respect to the DOM, the same technique yields a direction as well, with a typical zenith angle resolution of 15° (68% C.L.) in the sample presented here. Outgoing muon tracks are identified by inverting the incoming-track veto of Sec. II B as shown in Fig. 3c and classifying events with more than 10 photons in the detection window of an outgoing track as track-like. 35% (60%) of CC ν_μ events from the conventional atmospheric (E^{-2} astrophysical) spectrum satisfy this criterion; in the remaining events, the outgoing muon escapes the instrumented volume without being detected, and the event is mis-classified as a cascade. The reverse case is much rarer: 0.001% (3%) of NC ν_μ events from the conventional atmospheric (E^{-2} astrophysical) spectrum are

mis-classified as tracks. For track-like events the zenith angle is taken from the best-fit outgoing track, as the large displacement of the associated photons from the neutrino interaction vertex provides a better constraint than the initial cascade. Explicitly retaining these track-like events, rather than rejecting them with cuts designed to select cascade events, provides a built-in control sample that we use to check our understanding of the selection's neutrino acceptance.

Conventional atmospheric neutrinos are produced in the decays of charged pions and charged and neutral kaons in the atmosphere. Since these mesons are relatively long-lived, they are more likely to re-interact and lose energy than to decay to produce neutrinos. This competition affects both the deposited energy and the zenith angle distributions. The neutrino energy spectrum above 1 TeV is one power in energy steeper than that of the input cosmic ray spectrum, causing the deposited energy distribution to peak at low energies. The flux is largest at the horizon where the average density of the atmosphere along the air shower axis is smallest [55], causing the reconstructed zenith angle distribution to peak at the horizon as well. In the southern sky these effects are further enhanced by accompanying muons produced in the same air shower: they trigger the veto, removing high-energy, down-going atmospheric neutrino events from the sample [54]. The veto removes ν_μ more efficiently than ν_e , reducing the observable conventional atmospheric neutrino flux to the sub-dominant ν_e component at sufficiently high energies and small zenith angles.

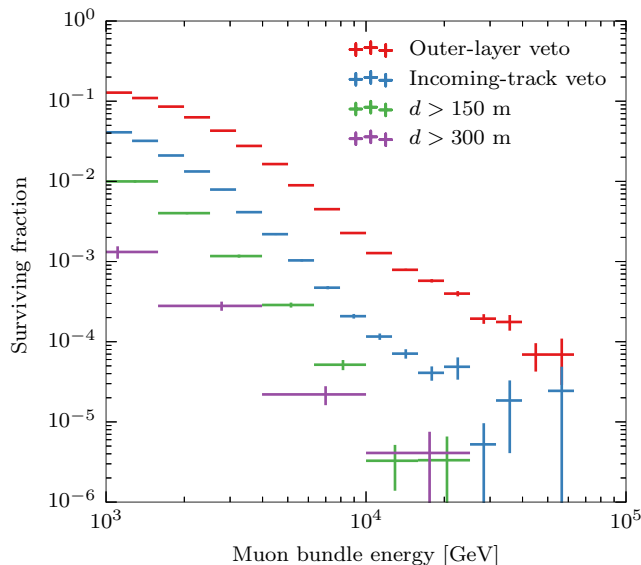


FIG. 4. Fraction of pre-selected penetrating muon background events (Sec. II A) that pass the veto conditions (Sec. II B), derived from MC simulation. The outer-layer veto reduces the rate of the highest-energy muons by 10^4 , but degrades rapidly at lower energies. The incoming-track veto scales in a similar way with respect to energy, but is more sensitive because it considers isolated photon detections. In contrast to the outer-layer veto, its efficiency also improves with increasing distance d from the detector border of the reconstructed vertex.

In this analysis, the flux model for conventional atmospheric neutrinos is taken from a parametrization of the calculation of [19], corrected to account for the cosmic ray flux of [76] as described in [53] and for the fraction of atmospheric neutrinos that are vetoed [57] by accompanying muons. These fluxes are shown in the upper two panels of Fig. 6.

Atmospheric neutrinos produced in the decays of charmed mesons behave differently. The lifetimes of charmed mesons are extremely short, so they nearly always decay promptly before re-interacting, producing an isotropic neutrino flux with nearly the same spectral index as that of the primary cosmic rays. Since neutrinos with accompanying muons are vetoed in the event selection, the observable flux is depleted in the southern sky. The overall suppression is weaker than for conventional atmospheric neutrinos because of the larger fraction of ν_e . The flux model for prompt atmospheric neutrinos is taken from a parameterization of the calculation of [28] with corrections for the cosmic ray flux and veto passing fraction. These fluxes are shown in the lower two panels of Fig. 6.

The events that pass the final selection include a small but nearly irreducible background of penetrating atmospheric muons that go undetected before depositing a large fraction of their energy in the glacial ice in a single, catastrophic loss. These events come exclusively

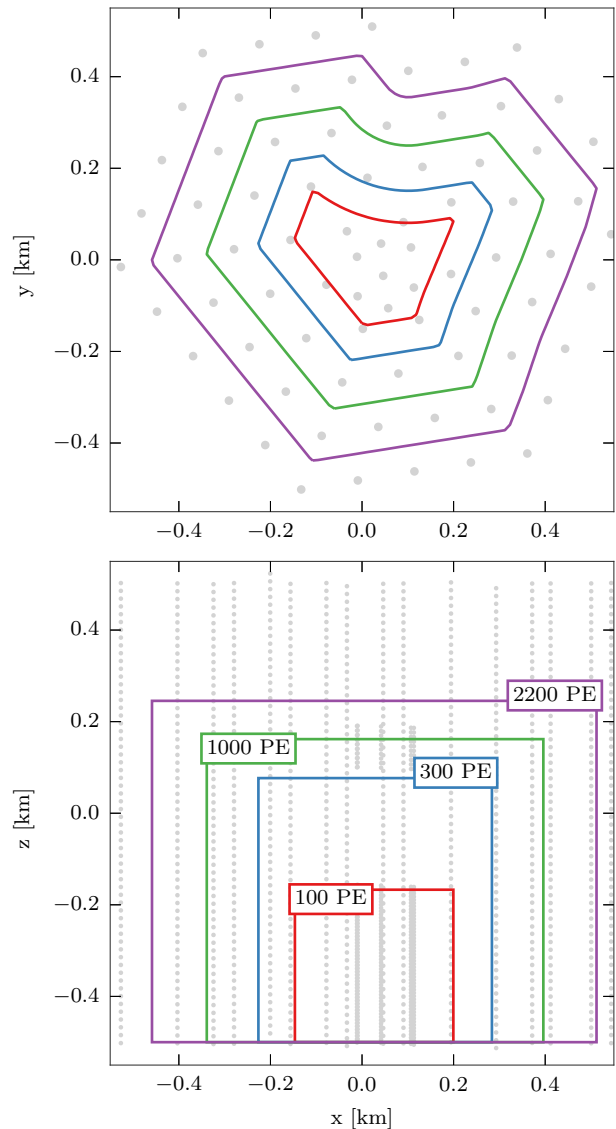


FIG. 5. Fiducial volume scaling function evaluated at four different photon counts. Top: Overhead view, showing the positions of the IceCube strings and the boundaries of the fiducial volume for events with a given total photon count. Bottom: Side view, showing the modules along strings.

from the southern sky because muons cannot penetrate the bulk of the Earth, and are sharply peaked at the deposited-energy threshold of the selection because the veto removes muons with increasing efficiency at higher energies. The flux model for penetrating atmospheric muons is taken from a parametrization of CORSIKA [77] air-shower simulations with the cosmic ray flux parameterization of [76], using the sum of muons from the decays of light hadrons predicted in SIBYLL [78] and from the decays of charmed hadrons predicted in DPMJET [79] to obtain an upper bound on the underground flux of single muons. This combined model predicts a total of 14 penetrating muon events in the sample.

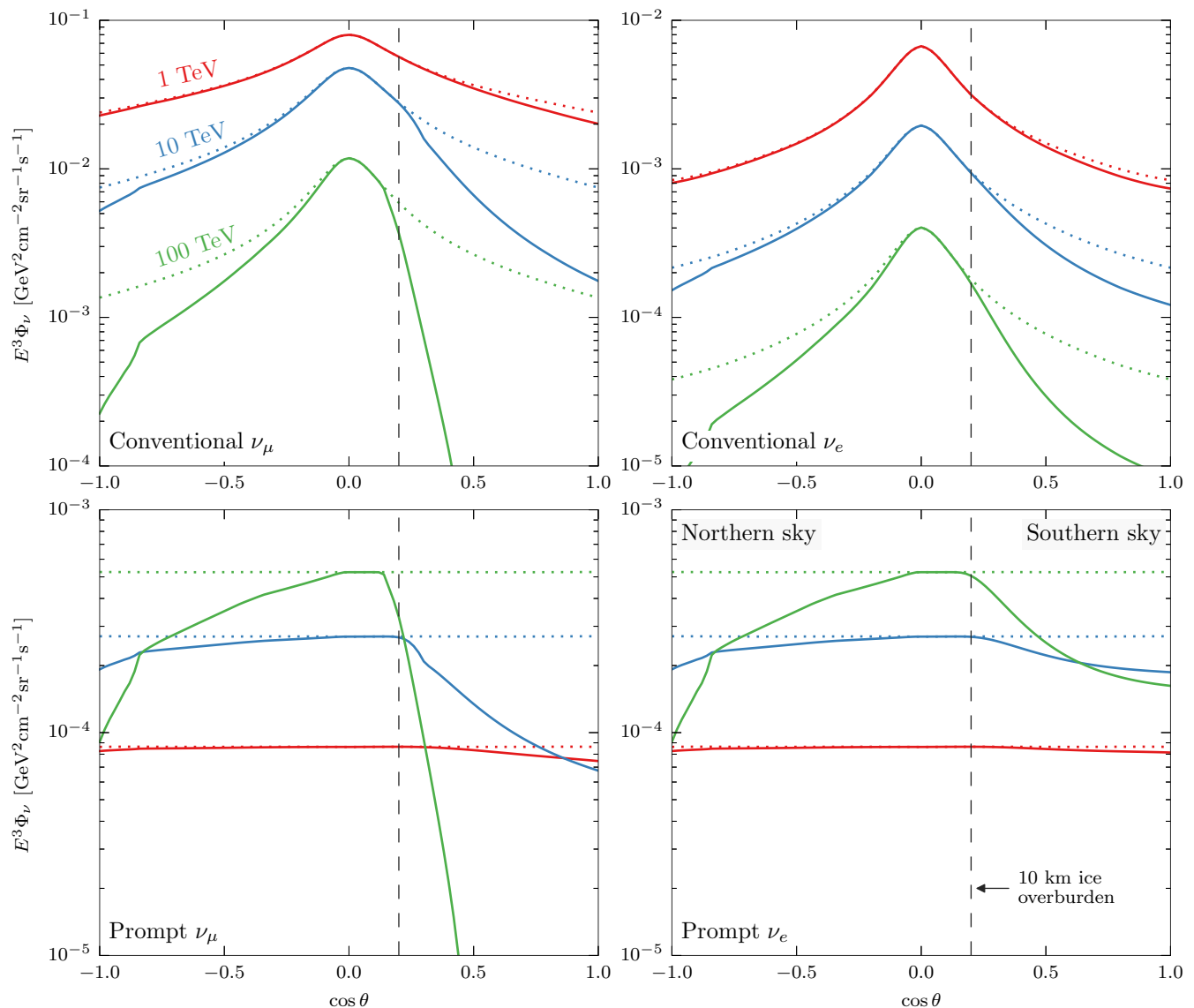


FIG. 6. Atmospheric neutrino flux models used in this analysis. The dotted lines in each panel show the neutrino fluxes at Earth’s surface as a function of true zenith angle at 1, 10, and 100 TeV. The conventional fluxes are taken from [19] and the prompt flux from [28]; both were corrected to account for the cosmic ray flux of [76]. The solid lines show the fluxes of ν_μ and ν_e that can be observed as isolated neutrino interactions in IceCube. The observable fluxes are suppressed in the northern sky ($\cos \theta \leq 0.2$, to the left of the vertical dashed line) by absorption in the Earth, especially in its much denser core ($\cos \theta < -0.8$) [65], and in the southern sky ($\cos \theta > 0.2$, to the right of the line) by self-veto by accompanying muons [57]. Astrophysical neutrinos are absorbed in the Earth as well, but are never accompanied by muons.

Overlaid on these atmospheric components is a flux of high-energy neutrinos of astrophysical origin. Their energy distribution is harder than those of any of the other sources of neutrinos, and we found that they are the dominant source of events with more than 100 TeV deposited energy [6, 7]. The Earth absorbs a significant fraction of upward-going neutrinos above 100 TeV [65], so the highest-energy of these are concentrated around the horizon and in the southern sky. Since the sources of these neutrinos are unknown, the shape of their energy and angular distribution cannot be predicted exactly, and

given the limited number of neutrino events that can be detected, only very simple models can be tested. Neutrinos associated with the extragalactic sources of the highest-energy cosmic rays are assumed to be isotropically distributed and follow a power law energy distribution of approximately E^{-2} [60] and arrive at the Earth as equal parts ν_e , ν_μ , and ν_τ due to oscillations [62]. We parameterize the diffuse astrophysical neutrino flux as

$$\Phi_{\text{astro}} = \Phi_0 \left(\frac{E}{E_0} \right)^{-\gamma}, \quad (1)$$

where Φ_0 is the $\nu + \bar{\nu}$ flux for each flavor at $E_0 = 10^5$ GeV in units of $\text{GeV}^{-1} \text{cm}^{-2} \text{sr}^{-1} \text{s}^{-1}$ and γ is the spectral index⁵. More generally, γ can be allowed to vary to account for the spectra expected from specific classes of sources, for example TeV photon emission from active galactic nuclei ($2.2 \lesssim \gamma \lesssim 2.6$) [4] or interactions of cosmic rays with dense gas clouds while magnetically confined in starburst galaxies ($2.0 \lesssim \gamma \lesssim 2.25$) [46].

Figure 7 shows the average deposited energy distributions expected from the northern and southern skies from the sources of neutrinos presented above. For the purposes of this analysis the southern sky extends only to 80° instead of the geometric horizon, since the ~ 10 kilometers water-equivalent of overburden at this zenith angle are already sufficient to remove the vast majority of atmospheric muons that would otherwise veto atmospheric neutrino events (see Fig. 6). Conventional atmospheric neutrinos are concentrated at deposited energies of a few TeV and in the northern sky around the geometric horizon; the smaller contribution above the horizon in the southern sky is further suppressed by vetoing muons (see Fig. 6). Since conventional atmospheric neutrinos have the largest fraction of ν_μ , they represent the largest contribution to the track-like portion of the data sample. The fraction of events in the track sample provides another constraint on the conventional atmospheric flux in addition to the deposited-energy and zenith distributions. The astrophysical component, shown as an isotropic flux with a normalization at the best fit of [7], dominates above 100 TeV in the northern and 30 TeV in the southern sky. The prompt atmospheric component, shown with a normalization at the previously-published upper limit of 3.8 [53], never provides a dominant contribution to the observed event rate. Instead, a large prompt component appears as an excess over the conventional atmospheric and astrophysical components in the northern sky in the 30–60 TeV region that is not matched in the southern sky. While the exact cross-over energies depend on the normalization and spectral index of the astrophysical component, the ordering of the energy ranges where each component can be constrained is generic.

The parameters of the model that best fit the observed data are determined through a binned likelihood fit. In this procedure, the data sample is binned in the three observables: reconstructed deposited energy, reconstructed zenith angle, and presence of a detectable outgoing track. The observed count n_i in each bin i is compared to a model that predicts the mean count rate λ_i in each bin through a Poisson likelihood function

$$L = \prod_{\text{bins } i} \frac{e^{-\lambda_i} \lambda_i^{n_i}}{n_i!}. \quad (2)$$

⁵ Equivalently, $E^2 \Phi_{\text{astro}} = \Phi_0 \times (10^{10} \text{ GeV}^2) \times \left(\frac{E}{E_0}\right)^{2-\gamma}$

The mean rates λ_i are computed by applying the event selection to simulated data and binning the observables of the surviving events in the same way as the experimental data, weighted according to the set of flux models under consideration. This convolves the flux model with the detector response to obtain observable distributions, a procedure known as forward folding. The model is fit to the data by varying its parameters until (2) is maximized.

The 68% confidence ranges on each model parameter are obtained from a likelihood-ratio test. To test whether a value of one parameter can be rejected at the desired confidence level, the parameter is constrained to that value while all other parameters are varied to maximize the conditional likelihood. The ratio between this conditional likelihood maximum and the global maximum is the profile likelihood. It can be used to construct a test statistic

$$-2\Delta \ln L = -2(\ln L - \ln L_{\text{max}}) \quad (3)$$

whose distribution approaches that of a χ^2 with 1 degree of freedom in the large-sample limit [80]. If $-2\Delta \ln L > 1$ (2.71), then the tested value of the model parameter is rejected at more than 68% (90%) confidence⁶.

IV. RESULTS

283 cascade and 105 track events passed the final selection criteria in 641 days of data-taking. Of those 388 events, 106 deposited more than 10 TeV at the cascade vertex, and 9 deposited more than 100 TeV. At high energies the selection overlaps nearly completely with the selection of [6]: 7 of the 9 events depositing more than 100 TeV were also in the previous selection.

The likelihood-fit approach described above was used to determine the fluxes of neutrinos and muons compatible with the observed events. In the first fit, the normalizations of the penetrating atmospheric muon component, the conventional and prompt atmospheric neutrino components, as well as the per-flavor normalization Φ_0 and spectral index γ of the astrophysical component were allowed to vary freely, resulting in the best-fit parameters shown in Tab. I. Figure 8 shows the deposited energy spectra corresponding to the best-fit model parameters. Figure 9 shows the zenith angle distributions of the sample with different energy thresholds.

This simple model does not describe the data perfectly. There is a notable departure in the southern sky around 30 TeV. However, the excess is not statistically

⁶ The test statistic does not necessarily follow a χ^2 distribution when the sample size is finite or a parameter is close to a bound. In such cases the exact confidence level can be derived numerically from Monte Carlo trials. In this analysis, however, the exact confidence intervals were found to be only slightly smaller than intervals derived from the χ^2 approximation.

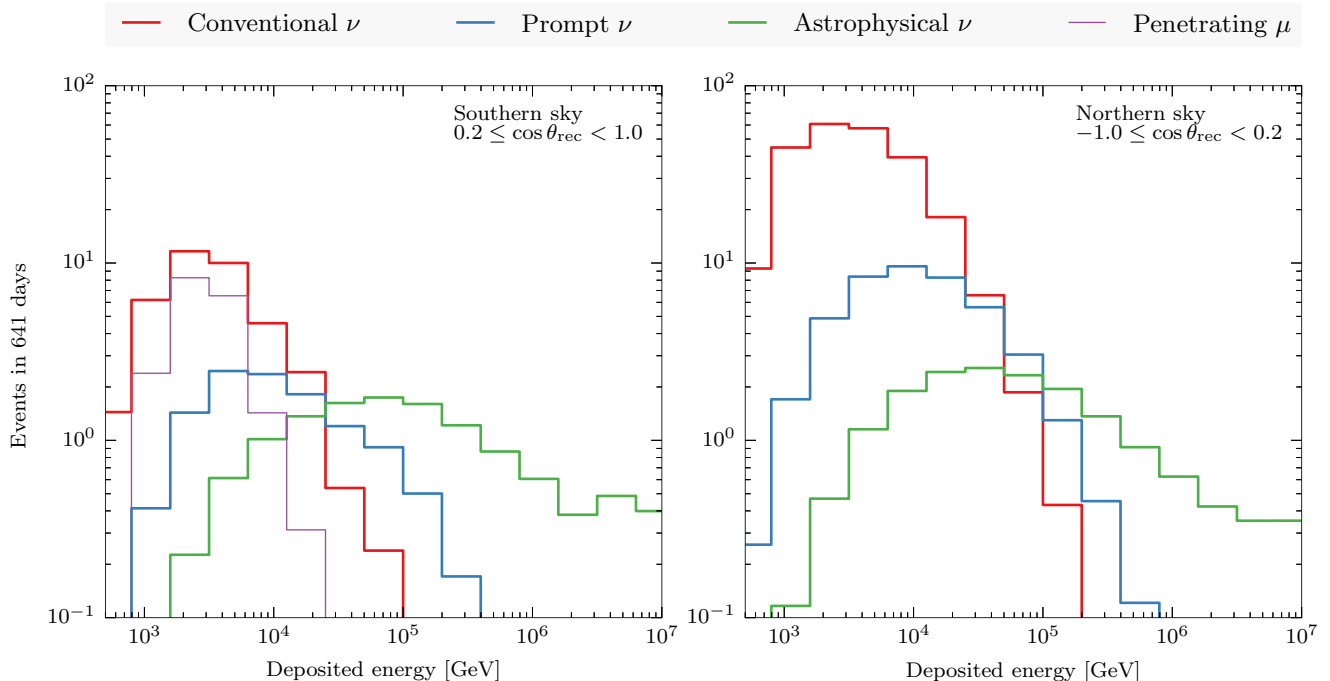


FIG. 7. Average deposited-energy spectra expected from the various sources of neutrinos in this analysis from the southern and northern skies. The conventional atmospheric component corresponds to the calculation of [19], with corrections for the knee of the cosmic-ray spectrum and the fraction vetoed by accompanying muons, while the prompt component corresponds to the calculation of [28] with similar corrections, but with the normalization taken from the previously-published upper limit of 3.8 [53]. The astrophysical component corresponds to Eq. (1) with $\Phi_0 = 10^{-18} \text{ GeV}^{-1} \text{ cm}^{-2} \text{ sr}^{-1} \text{ s}^{-1}$ and $\gamma = 2$.

TABLE I. Best fit parameters and number of events attributable to each component. The normalizations of the atmospheric fluxes are relative to the models described in Sec. III. The per-flavor normalization Φ_0 and spectral index γ of the astrophysical flux are defined in Eq. (1); the fit to the astrophysical flux is sensitive to $25 \text{ TeV} < E_\nu < 1.4 \text{ PeV}$. The two-sided error ranges given are 68% confidence regions in the χ^2 approximation; upper limits are at 90% confidence. The goodness-of-fit p-value for this model is 0.2.

Parameter	Best-fit value	No. of events
Penetrating μ flux	$1.73 \pm 0.40 \Phi_{\text{SIBYLL+DPMJET}}$	30 ± 7
Conventional ν flux	$0.97_{-0.03}^{+0.10} \Phi_{\text{HKMS}}$	280_{-8}^{+28}
Prompt ν flux	$< 1.52 \Phi_{\text{ERS}} \text{ (90\% CL)}$	< 23
Astrophysical Φ_0	$2.06_{-0.26}^{+0.35} \times 10^{-18}$ $\text{GeV}^{-1} \text{ cm}^{-2} \text{ sr}^{-1} \text{ s}^{-1}$	87_{-10}^{+14}
Astrophysical γ	2.46 ± 0.12	

significant; correlated fluctuations of the observed size or greater are expected from a smooth underlying power-law spectrum in 5% of experiments. The events in the energy and zenith region of the excess are overwhelmingly cascade-like and display no signs of early hits from penetrating atmospheric muons. Their rate far exceeds that expected from penetrating muon background and conventional atmospheric neutrinos (~ 1 event per year),

and their distribution in time and within the fiducial volume is compatible with a uniform one. Known sources of systematic uncertainty in the neutrino acceptance of the detector, like the optical properties of the glacial ice or the optical efficiency of the DOM, are unable to create structure in the observed energy distribution. At present, we interpret this as a statistical fluctuation. We expect that future searches using more years of data will help constrain the cause of the excess, either by reducing its significance or by strengthening it enough that definitive statistical statements can be made.

The spectral index of 2.46 needed to explain the low-energy data has implications for the underlying neutrino production mechanism. As pointed out in [81], pp interactions produce neutrinos and γ -rays that follow the same scale-free power-law spectrum, and the γ spectra from pp interactions at $\sim \text{GeV}$ energies can be extrapolated to the TeV range where IceCube observes neutrinos. This extrapolation argument does not apply to $p\gamma$ interactions. If the diffuse extragalactic γ background measured by Fermi-LAT is due to extragalactic pp interactions in optically thin regions, then the spectral index of the associated neutrino spectrum must be smaller than 2.2. [81]. The data presented here indicate that the neutrino spectrum is softer than $E^{-2.2}$ with 90% confidence

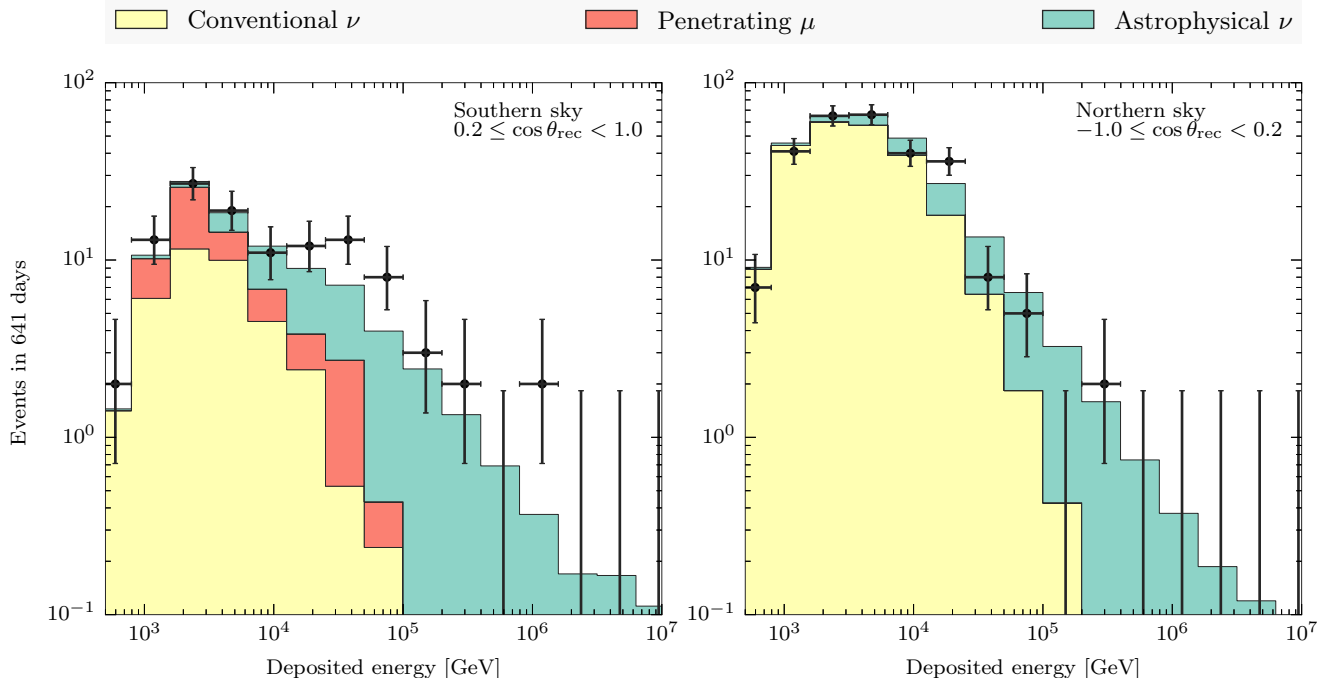


FIG. 8. Deposited energy spectra from the northern and southern skies (points) with the best-fit combination of atmospheric and astrophysical contributions from Table I. Below 3 TeV, the events observed from the northern sky are adequately explained by conventional atmospheric neutrinos. In the same energy range in the southern sky, penetrating atmospheric muons account for the remaining events. Above 10 TeV, an extra component is required to account for the observed high-energy events, especially those in the southern sky. Since atmospheric neutrinos of any kind are often vetoed by accompanying muons, the excess is best explained by astrophysical neutrinos. We interpret the excess over the best-fit sum around 30 TeV as a statistical fluctuation.

(see Fig. 11a), implying that one of these assumptions is violated.

All of the parameters in Tab. I are correlated except for the conventional atmospheric neutrino flux normalization. The latter is determined mostly by the northern-sky data below 10 TeV deposited energy, where the contributions of the other components are negligible, and is compatible with the expected normalization [19] to within statistical errors, providing a useful check of the neutrino acceptance calculated from simulation. Similarly, the low-energy component provides a verification of the atmospheric neutrino veto independent of the observed astrophysical excess, as shown in Fig. 10. The prompt atmospheric neutrino flux, on the other hand, can provide a significant contribution to the overall event rate between 10 and 100 TeV deposited energy, but has no region where it contributes exclusively. Its inferred normalization depends on assumptions about the astrophysical neutrino flux. The correlations between the astrophysical and prompt atmospheric components are shown in Fig. 11. Since the power-law index of the astrophysical flux is constrained primarily by the large number of events below the pivot point at 100 TeV, the normalization and index are correlated. Similarly, the prompt

normalization is correlated with the astrophysical index; as the index is forced to smaller values, a larger prompt flux is required to explain the data between 10 and 100 TeV deposited energy. The normalization of the penetrating muon component is constrained by the excess of southern-sky data over the conventional atmospheric neutrino expectation below a few TeV, and is weakly correlated with it (not shown).

These correlations would not be problematic if the model of the astrophysical flux were exact, but since its sources are not known, any single model will necessarily be an approximation. It is useful to examine how assumptions about astrophysical models affect the upper limit on the prompt atmospheric flux normalization. The first assumption made is that the astrophysical flux must follow a single power-law energy distribution. This assumption can be relaxed by describing the astrophysical neutrino flux with a piecewise constant function of neutrino energy as shown in Fig. 12. The observed excess in the deposited energy spectrum is reflected in a corresponding excess in the neutrino energy spectrum, and the additional freedom granted to the astrophysical component weakens the 90% upper limit on the prompt atmospheric flux from 1.52 to 1.75 times the prediction of

[28]. This remaining limit is driven primarily by the assumption that the astrophysical neutrino flux is isotropic. If this assumption is weakened by allowing the astrophysical fluxes that contribute to the northern- and southern-sky data to vary independently, the limit relaxes further to 3.69. While this limit is not meaningfully smaller than the previously published limit of 3.8 [53], it involves many fewer assumptions about the nature of the astrophysical neutrino background.

V. CONCLUSION

In the analysis presented here, we used a veto-based technique to isolate 388 events starting in the IceCube instrumented volume and depositing more than 1 TeV from 641 days of data, of which 92% were neutrino events. Astrophysical neutrino candidates were observed in the southern sky with energies as low as 10 TeV, far below the threshold of the previous high-energy starting event analysis [6, 7] and in a region inaccessible to the traditional up-going track analysis [53]. We characterized the contributions of penetrating atmospheric muons, conventional and prompt atmospheric neutrinos, and astrophysical neutrinos to the data sample using a likelihood fit to the distributions of deposited energy and zenith angle for cascade and starting-track events.

The analysis yielded new information about the behavior of the neutrino spectrum between 10 and 100 TeV. If the energy spectrum of the astrophysical neutrinos is a single power law, then it must have a spectral index of 2.46 ± 0.12 , softer than the typical E^{-2} benchmark spectrum. The $\gamma = 2$ hypothesis can be rejected with 99% confidence under this assumption. The new constraint on the spectral index is due primarily to the lower deposited-energy threshold of this analysis. If the deposited-energy threshold is raised to 60 TeV (corresponding to sensitivity for $E_\nu > 100$ TeV), then the best-fit spectral index hardens to 2.26 ± 0.35 , compatible with the previous high-energy result [7]. The statistically insignificant excess that appeared in the down-going data near 30 TeV, a region where atmospheric leptons are heavily suppressed, had only a minor influence on the inferred spectral index of the astrophysical neutrinos. If we force the spectral index to $\gamma = 2$, then the per-flavor normalization Φ_0 (cf. Eq. (1)) drops to $1.22 \pm 0.5 \times 10^{-18} \text{ GeV}^{-1} \text{ cm}^{-2} \text{ sr}^{-1} \text{ s}^{-1}$, consistent with the previously published 90% C.L. upper limit of 1.44 derived from northern-sky ν_μ events [53]. At the same time, we searched for atmospheric neutrinos from charmed meson decay. No such component was observed, and we placed upper limits on their flux. These limits depend strongly on assumptions about the astrophysical neutrino background, and range from 1.52 times the prediction from perturbative QCD [28] at 90% confidence when the astrophysical flux is assumed to follow a single isotropic power-law distribution to 3.69 times the prediction when it is described with a piecewise constant

function of energy and zenith angle.

The constraints on the astrophysical flux are currently limited by the small number of observed high-energy events, making it difficult to draw strong inferences about the classes of cosmic-ray accelerators from the characteristics of the associated neutrino spectrum. Beyond astrophysical considerations, the inability to model the astrophysical flux precisely and reliably extrapolate its angular and energy distribution to lower energies impedes any attempt to measure the level of charmed-meson production in air showers via high-energy neutrinos. Both of these problems may be approached with more and different data. IceCube will continue to collect data, and future iterations of this analysis will be able to use at least twice as many high-energy neutrino events to constrain the energy spectrum and eventually possible anisotropies of the astrophysical neutrino flux. In addition to better modeling of the astrophysical background, sensitivity to charmed meson production in the atmosphere will be improved by analyzing penetrating muon events jointly with neutrino events. These are produced in the same decays as prompt muon neutrinos, but have no astrophysical background to contend with.

ACKNOWLEDGMENTS

We acknowledge the support from the following agencies: U.S. National Science Foundation-Office of Polar Programs, U.S. National Science Foundation-Physics Division, University of Wisconsin Alumni Research Foundation, the Grid Laboratory Of Wisconsin (GLOW) grid infrastructure at the University of Wisconsin - Madison, the Open Science Grid (OSG) grid infrastructure; U.S. Department of Energy, and National Energy Research Scientific Computing Center, the Louisiana Optical Network Initiative (LONI) grid computing resources; Natural Sciences and Engineering Research Council of Canada, WestGrid and Compute/Calcul Canada; Swedish Research Council, Swedish Polar Research Secretariat, Swedish National Infrastructure for Computing (SNIC), and Knut and Alice Wallenberg Foundation, Sweden; German Ministry for Education and Research (BMBF), Deutsche Forschungsgemeinschaft (DFG), Helmholtz Alliance for Astroparticle Physics (HAP), Research Department of Plasmas with Complex Interactions (Bochum), Germany; Fund for Scientific Research (FNRS-FWO), FWO Odysseus programme, Flanders Institute to encourage scientific and technological research in industry (IWT), Belgian Federal Science Policy Office (Belspo); University of Oxford, United Kingdom; Marsden Fund, New Zealand; Australian Research Council; Japan Society for Promotion of Science (JSPS); the Swiss National Science Foundation (SNSF), Switzerland; National Research Foundation of Korea (NRF); Danish National Research Foundation, Denmark (DNRF)

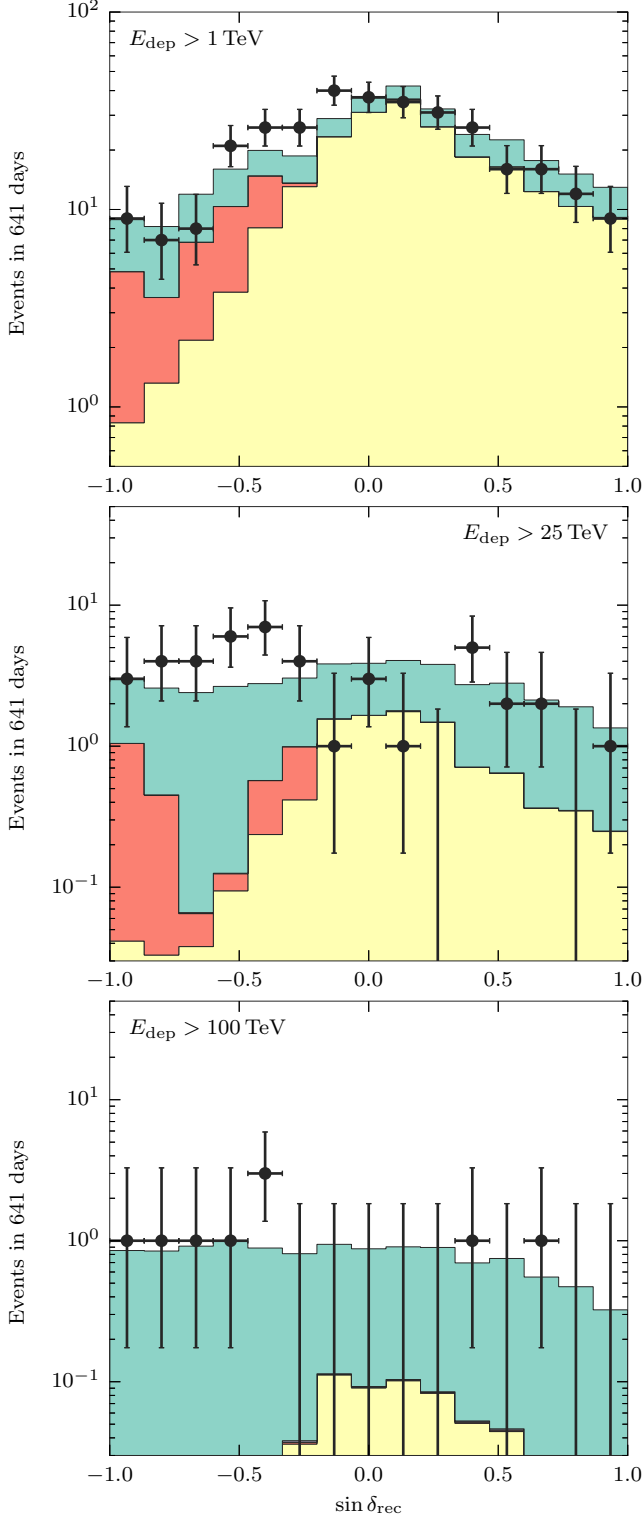


FIG. 9. Zenith angle distribution of events depositing more than 1, 25, and 100 TeV (points) with the best-fit combination of atmospheric and astrophysical contributions from Table I, using the same color scheme as in Fig. 8. At the lowest energies the sample is concentrated at the horizon, as expected from conventional atmospheric neutrinos. The astrophysical component contributes significantly to the sample above 25 TeV, and the bulk of the sample is down-going. By 100 TeV only the astrophysical component remains, and the up-going flux is suppressed by absorption in the Earth.

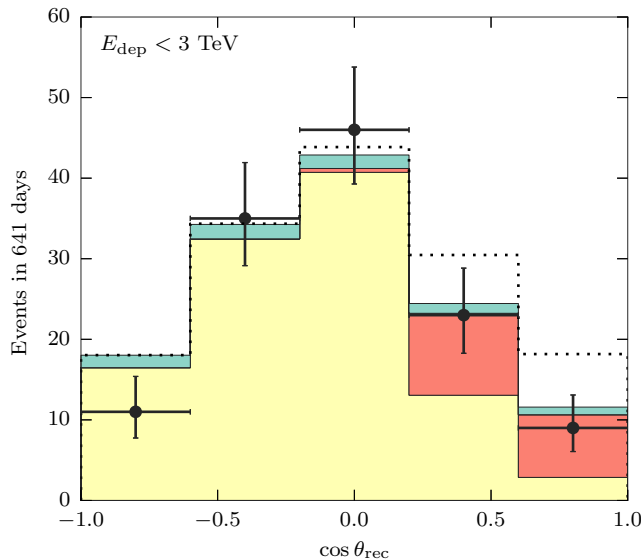
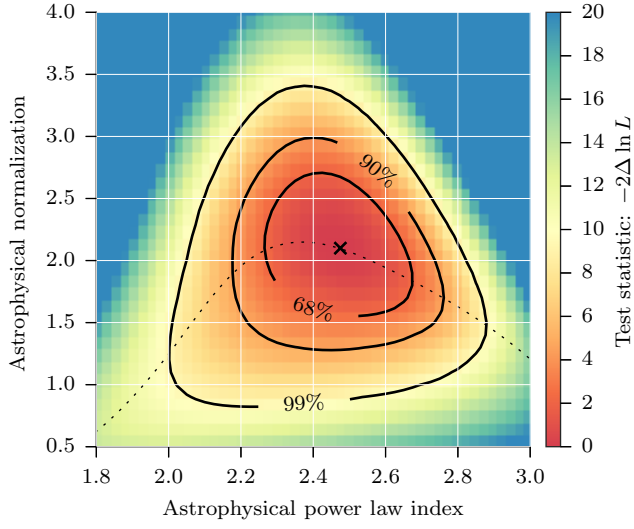


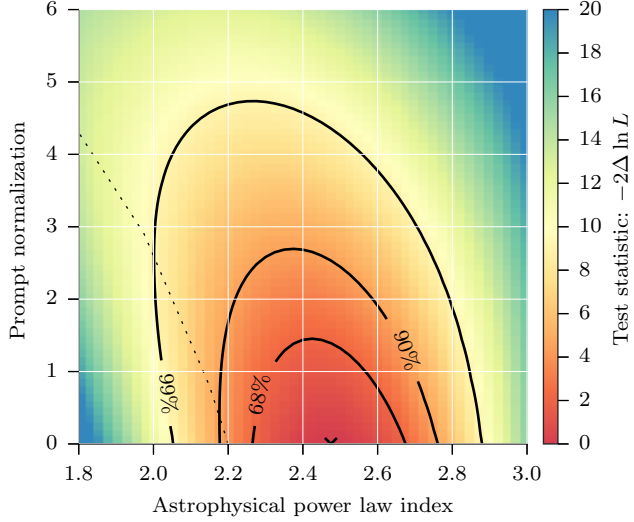
FIG. 10. Verification of atmospheric neutrino veto with low-energy data. The points show events depositing less than 3 TeV, while the stacked histograms show the expected contributions from conventional atmospheric neutrinos, penetrating muons, and the negligible contribution of astrophysical neutrinos, using the color scheme of Fig. 8. These match the observed data much better than the dotted line, which shows the number of events that would be collected if atmospheric neutrinos were never vetoed by accompanying muons.

-
- [1] T. K. Gaisser, F. Halzen, and T. Stanev, *Physics Reports* **258**, 173 (1995), hep-ph/9410384.
- [2] J. G. Learned and K. Mannheim, *Annual Review of Nuclear and Particle Science* **50**, 679 (2000).
- [3] F. Halzen and D. Hooper, *Reports on Progress in Physics* **65**, 1025 (2002), astro-ph/0204527.
- [4] J. K. Becker, *Physics Reports* **458**, 173 (2008).
- [5] R. Abbasi et al. (IceCube Collaboration), *Nuclear Instruments and Methods A* **601**, 294 (2009).
- [6] M. Aartsen et al. (IceCube Collaboration), *Science* **342** (2013), 10.1126/science.1242856.
- [7] M. Aartsen et al. (IceCube Collaboration) ((IceCube Collaboration)), *Phys. Rev. Lett.* **113**, 101101 (2014).
- [8] R. Laha, J. F. Beacom, B. Dasgupta, S. Horiuchi, and K. Murase, *Phys. Rev. D* **88**, 043009 (2013).
- [9] I. Cholis and D. Hooper, *Journal of Cosmology and Astroparticle Physics* **6**, 030 (2013), arXiv:1211.1974 [astro-ph.HE].
- [10] W. Winter, *Phys. Rev. D* **88**, 083007 (2013), arXiv:1307.2793 [astro-ph.HE].
- [11] O. E. Kalashev, A. Kusenko, and W. Essey, *Phys. Rev. Lett.* **111**, 041103 (2013), arXiv:1303.0300 [astro-ph.HE].
- [12] E. Roulet, G. Sigl, A. van Vliet, and S. Mollerach, *Journal of Cosmology and Astroparticle Physics* **1**, 028 (2013), arXiv:1209.4033 [astro-ph.HE].
- [13] F. W. Stecker, ArXiv e-prints (2013), arXiv:1305.7404 [astro-ph.HE].
- [14] H.-N. He, T. Wang, Y.-Z. Fan, S.-M. Liu, and D.-M. Wei, *Phys. Rev. D* **87**, 063011 (2013), arXiv:1303.1253 [astro-ph.HE].
- [15] L. A. Anchordoqui, H. Goldberg, M. H. Lynch, A. V. Olinto, T. C. Paul, and T. J. Weiler, ArXiv e-prints (2013), arXiv:1306.5021 [astro-ph.HE].
- [16] M. C. Gonzalez-Garcia, F. Halzen, and V. Niro, ArXiv e-prints (2013), arXiv:1310.7194 [astro-ph.HE].
- [17] S. Razzaque, *Phys. Rev. D* **88**, 081302 (2013), arXiv:1309.2756 [astro-ph.HE].
- [18] T. K. Gaisser, S. A. Bludman, H. Lee, and T. Stanev, *Phys. Rev. Lett.* **51**, 223 (1983).
- [19] M. Honda, T. Kajita, K. Kasahara, S. Midorikawa, and T. Sanuki, *Phys. Rev. D* **75**, 043006 (2007).
- [20] C. Gonzalez-Garcia, M. Maltoni, and J. Rojo, *Journal of High Energy Physics* **10**, 075 (2006), hep-ph/0607324.
- [21] P. Lipari, M. Lusignoli, and D. Meloni, *Phys. Rev. D* **75**, 123005 (2007), arXiv:0704.0718.
- [22] A. Fedynitch, J. Becker Tjus, and P. Desiati, *Phys. Rev. D* **86**, 114024 (2012).
- [23] V. S. Berezinsky, D. Cline, and D. N. Schramm, *Physics Letters B* **78**, 635 (1978).
- [24] L. V. Volkova, *International Cosmic Ray Conference* **7**, 22 (1983).
- [25] L. V. Volkova, *Physics Letters B* **462**, 211 (1999).
- [26] G. Gelmini, P. Gondolo, and G. Varieschi, *Phys. Rev. D* **61**, 056011 (2000), hep-ph/9905377.
- [27] A. Martin, M. Ryskin, and A. Stasto, *Acta Physica Polonica B* **34**, 3273 (2003).

- [28] R. Enberg, M. H. Reno, and I. Sarcevic, *Phys. Rev. D* **78**, 043005 (2008).
- [29] M. H. Reno, in *American Institute of Physics Conference Series*, American Institute of Physics Conference Series, Vol. 1560, edited by B. Fleming (2013) pp. 350–354.
- [30] P. L. Biermann, in *Cosmic Gamma Rays and Cosmic Neutrinos*, edited by M. M. Shapiro and J. P. Wefel (1989) pp. 21–37.
- [31] W. Michalak, J. Wdowczyk, and A. W. Wolfendale, *Journal of Physics G Nuclear Physics* **16**, 1917 (1990).
- [32] F. W. Stecker, C. Done, M. H. Salamon, and P. Sommers, *Phys. Rev. Lett.* **66**, 2697 (1991).
- [33] L. Nellen, K. Mannheim, and P. L. Biermann, *Phys. Rev. D* **47**, 5270 (1993), hep-ph/9211257.
- [34] K. Mannheim, *Astroparticle Physics* **3**, 295 (1995).
- [35] F. W. Stecker and M. H. Salamon, *Space Science Reviews* **75**, 341 (1996), astro-ph/9501064.
- [36] J. P. Rachen and P. Mészáros, *Phys. Rev. D* **58**, 123005 (1998), astro-ph/9802280.
- [37] P. Mészáros and E. Waxman, *Phys. Rev. Lett.* **87**, 171102 (2001), astro-ph/0103275.
- [38] A. Mücke, R. J. Protheroe, R. Engel, J. P. Rachen, and T. Stanev, *Astroparticle Physics* **18**, 593 (2003), astro-ph/0206164.
- [39] J. K. Becker, P. L. Biermann, and W. Rhode, *Astroparticle Physics* **23**, 355 (2005), astro-ph/0502089.
- [40] F. W. Stecker, *Phys. Rev. D* **72**, 107301 (2005).
- [41] B. Eichmann, R. Schlickeiser, and W. Rhode, *Astrophys. J.* **749**, 155 (2012).
- [42] E. Waxman and J. N. Bahcall, *Astrophys. J.* **541**, 707 (2000), hep-ph/9909286.
- [43] S. Razzaque, P. Mészáros, and E. Waxman, *Phys. Rev. D* **68**, 083001 (2003), astro-ph/0303505.
- [44] J. K. Becker, M. Stamatikos, F. Halzen, and W. Rhode, *Astroparticle Physics* **25**, 118 (2006), astro-ph/0511785.
- [45] K. Murase and S. Nagataki, *Phys. Rev. Lett.* **97**, 051101 (2006), astro-ph/0604437.
- [46] A. Loeb and E. Waxman, *Journal of Cosmology and Astroparticle Physics* **2006**, 003 (2006).
- [47] P. L. Biermann, B. B. Nath, L. I. Caramete, B. C. Harms, T. Stanev, and J. B. Tjus, *Monthly Notices of the RAS* **441**, 1147 (2014), arXiv:1403.3804 [astro-ph.CO].
- [48] J. Alvarez-Muñiz and F. Halzen, *ApJ Letters* **576**, L33 (2002), astro-ph/0205408.
- [49] D. Guetta and E. Amato, *Astroparticle Physics* **19**, 403 (2003), astro-ph/0209537.
- [50] F. Halzen, A. Kappes, and A. Ó Murchadha, *Phys. Rev. D* **78**, 063004 (2008), arXiv:0803.0314.
- [51] M. Mandelartz and J. Becker Tjus, *ArXiv e-prints* (2013), arXiv:1301.2437 [astro-ph.GA].
- [52] T. K. Gaisser, *Cosmic rays and particle physics* (Cambridge University Press, Cambridge and New York, 1990).
- [53] M. Aartsen et al. (IceCube Collaboration) (The IceCube Collaboration), *Phys. Rev. D* **89**, 062007 (2014), arXiv:1311.7048 [astro-ph.HE].
- [54] S. Schönert, T. K. Gaisser, E. Resconi, and O. Schulz, *Phys. Rev. D* **79**, 043009 (2009).
- [55] P. Lipari, *Astroparticle Physics* **1**, 195 (1993).
- [56] M. Aartsen et al. (IceCube Collaboration) (IceCube Collaboration), *Phys. Rev. Lett.* **110**, 151105 (2013).
- [57] T. K. Gaisser, K. Jero, A. Karle, and J. van Santen, *Phys. Rev. D* **90**, 023009 (2014), arXiv:1405.0525.
- [58] J. Beringer et al. (Particle Data Group), *Phys. Rev. D* **86**, 010001 (2012).
- [59] E. Bugaev, V. Naumov, S. Sinegovsky, and E. Zaslavskaya, *Il Nuovo Cimento C* **12**, 41 (1989).
- [60] E. Waxman and J. Bahcall, *Phys. Rev. D* **59**, 023002 (1998).
- [61] J. G. Learned and S. Pakvasa, *Astroparticle Physics* **3**, 267 (1995).
- [62] S. Choubey and W. Rodejohann, *Phys. Rev. D* **80**, 113006 (2009).
- [63] R. Abbasi et al. (IceCube Collaboration), *Astroparticle Physics* **35**, 615 (2012).
- [64] M. Aartsen et al. (IceCube Collaboration), *Journal of Instrumentation* **9**, P03009 (2014).
- [65] R. Gandhi, C. Quigg, M. H. Reno, and I. Sarcevic, *Astroparticle Physics* **5**, 81 (1996).
- [66] J. Ahrens et al. (AMANDA Collaboration), *Nuclear Instruments and Methods A* **524**, 169 (2004).
- [67] M. Ackermann et al. (AMANDA Collaboration), *Astroparticle Physics* **22**, 127 (2004).
- [68] R. Abbasi et al. (AMANDA and IceCube Collaborations), *Astroparticle Physics* **34**, 420 (2011).
- [69] R. Abbasi et al. (IceCube Collaboration) (IceCube Collaboration), *Phys. Rev. D* **84**, 072001 (2011).
- [70] M. Aartsen et al. (IceCube Collaboration) ((IceCube Collaboration)), *Phys. Rev. D* **89**, 102001 (2014).
- [71] R. Abbasi et al. (IceCube Collaboration), *Nuclear Instruments and Methods A* **618**, 139 (2010).
- [72] A. Achterberg et al. (IceCube Collaboration), *Astroparticle Physics* **26**, 155 (2006).
- [73] M. A. et al (IceCube Collaboration) (IceCube Collaboration), *Phys. Rev. Lett.* **110**, 131302 (2013).
- [74] K. M. Górski, E. Hivon, A. J. Banday, B. D. Wandelt, F. K. Hansen, M. Reinecke, and M. Bartelmann, *The Astrophysical Journal* **622**, 759 (2005).
- [75] J. F. Beacom and J. Candia, *Journal of Cosmology and Astroparticle Physics* **2004**, 009 (2004).
- [76] T. K. Gaisser, *Astroparticle Physics* **35**, 801 (2012).
- [77] D. Heck, J. Knapp, J. Capdevielle, G. Schatz, and T. Thouw, *CORSIKA: A Monte Carlo Code to Simulate Extensive Air Showers*, Tech. Rep. FZKA 6019 (Forschungszentrum Karlsruhe, 1998).
- [78] E.-J. Ahn, R. Engel, T. K. Gaisser, P. Lipari, and T. Stanev, *Phys. Rev. D* **80**, 094003 (2009).
- [79] P. Berghaus, T. Montaruli, and J. Ranft, *Journal of Cosmology and Astroparticle Physics* **2008**, 003 (2008).
- [80] S. S. Wilks, *The Annals of Mathematical Statistics* **9**, 60 (1938).
- [81] K. Murase, M. Ahlers, and B. C. Lacki, *Phys. Rev. D* **88**, 121301 (2013), arXiv:1306.3417 [astro-ph.HE].
- [82] M. Aartsen et al. (IceCube Collaboration), *Phys. Rev. D* **88**, 112008 (2013).



(a) Likelihood profile in astrophysical power-law index γ and per-flavor normalization $\Phi_0/10^{-18} \text{ GeV}^{-1} \text{ cm}^{-2} \text{ sr}^{-1} \text{ s}^{-1}$. $E^{-2.5}$ is strongly favored over E^{-2} .



(b) Likelihood profile in astrophysical power-law index γ and prompt atmospheric neutrino flux normalization [28].

FIG. 11. Profile likelihood scans showing the correlation between the astrophysical power-law index and the normalizations of the astrophysical and prompt atmospheric components. In each plot, the colors show the test statistic (3), obtained by fixing the parameters shown on the axes and varying all others to obtain the conditional best fit. The x shows the best-fit point as in Tab. I and the contours show confidence regions in the χ^2 approximation [80] with 2 degrees of freedom. The thin dotted line shows the conditional best fit for each value of γ .

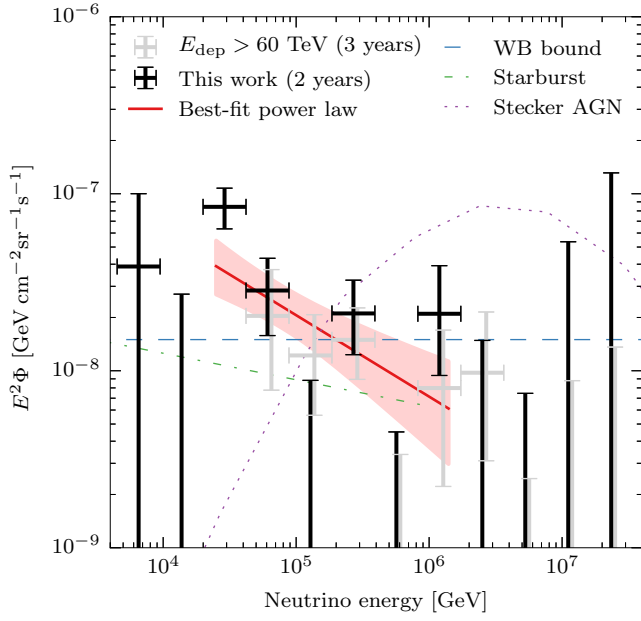


FIG. 12. Unfolding the non-atmospheric excess as piecewise-constant per-flavor fluxes $E^2\Phi$. The horizontal error bars show the range of primary neutrino energies that contribute to each bin, while the vertical error bars show the range of $E^2\Phi$ that change the $-2\Delta \ln L$ test statistic by less than 1. The black points show the fit to the data sample presented here; the light grey data points are from the 3-year data sample of [7], shifted slightly to the right for better visibility. Above the highest observed energy, the error bars provide upper limits on the flux; these are less constraining than the upper limits of [82] above 10 PeV. The thin lines show models for the diffuse astrophysical neutrino background: the upper bound from the total luminosity of EeV cosmic rays from [60] (blue), the starburst galaxy model of [46] (green), and the AGN core emission model of [40] (purple).